Applied Catalysis B: Environmental 182 (2016) 94–101

Contents lists available at ScienceDirect

Applied Catalysis B: Environmental

journal homepage: www.elsevier.com/locate/apcatb

Sintering and coking resistant core–shell microporous silica–nickel nanoparticles for CO methanation: Towards advanced catalysts production

Mattia A. Lucchini[a,b], Andrea Testino[a,*], Anastasios Kambolis[a,c], Christian Proff[a], Christian Ludwig[a,d]

[a] Paul Scherrer Institut, General Energy Research Department, CH-5232 Villigen PSI, Switzerland
[b] ETH Zürich, Department of Materials, Laboratory for Multifunctional Material, CH-8093 Zürich, Switzerland
[c] École Polytechnique Feídeírale de Lausanne (EPFL), Institut des Sciences et Ingeínierie Chimiques, CH-1015 Lausanne, Switzerland
[d] École Polytechnique Feídeírale de Lausanne (EPFL), ENAC – IIE, CH-1015 Lausanne, Switzerland

ARTICLE INFO

Article history:
Received 7 July 2015
Received in revised form 2 September 2015
Accepted 5 September 2015
Available online 9 September 2015

Keywords:
Anti sintering
Anti coking
Core shell nanoparticles
CO methanation
Nickel silica nanoparticles

ABSTRACT

Modern engineered materials have to be developed to address specific problems associated to chemical processes that directly affect our society. Catalysts are key materials used for large scale production of at least 90% of the everyday goods. Many energy transformation chains exist in which catalysts are used at relatively high temperature. Therefore, deactivation due to sintering and poisoning is a common phenomenon and often the reason for unsuccessful implementation of new catalytic processes. In this paper, a Ni-based catalyst for CO methanation is studied with the aim to address two specific issues, namely the sintering and the carbon deposition, which both hinder the stability and the efficiency of the catalyst over time. The engineered material is composed by a Ni core of about 170 nm protected by a 30–40 nm microporous SiO_2 layer. The porous layer allows the gases to permeate and completely inhibits particle–particle sintering. The experimental evidences demonstrate that even in the presence of 2000 ppm of C_2H_4 no carbon deposition occurs on the catalyst surface. The reported materials show outstanding properties paving the way to a new class of advanced functional material with improved catalytic activity and stability.

1. Introduction

The predictable decrease of fossil fuels reserves combined with the environmental drawbacks related to their use, the restricted legislations on emission, and the political instabilities in the producing countries, represent a clear driving force towards a more efficient exploitation of our current energy resources. Therefore, scientists in both universities and industries face common challenges: exploring new technologies in order to improve our energy diversification, distribution, and storage strategies.

In this context, methane offers a series of advantages because of its low carbon to hydrogen ratio, the existence of a capillary pipeline which is fast expanding and is acting both as distribution grid and storage system. Today, a number of facilities are designed to use methane as energy source, such as turbines, vehicles, fuel cells, domestic equipment, and many others.

Methane-rich gas (SNG, synthetic natural gas) can be produced from CO, CO_2 and H_2 according to the following reactions:

$$3H_2 + CO \rightarrow CH_4 + H_2O \Delta H^\circ = -206\,kJ/mol \quad (1)$$

$$4H_2 + CO_2 \rightarrow CH_4 + 2H_2O \Delta H^\circ = -165\,kJ/mol \quad (2)$$

Reaction (2) is also known as Sabatier reaction. If the reactant gas mixture is produced from biomass, the overall energy transformation is carbon neutral [1]. To be injected into the grid, the produced SNG has to be purified (fuel upgrading) in order to remove unreacted gases such as H_2, CO, and CO_2, the by-product H_2O, and trace contaminants [2].

Reactions (1) and (2) are exothermic and competitive reactions can occur: to obtain high reaction yield and high selectivity toward methane, the process has to be conducted at low temperature and assisted by a catalyst.

Several catalytic systems have been proposed and studied for the CO methanation [3–5]. The most common systems are based on Ni or Ru [6,7]. Ru-based catalysts show better performance [8] but they are more prone to chemical poisoning and rather expensive. On the other hand, Ni-based catalysts are less active [9].

* Corresponding author.
E-mail address: andrea.testino@psi.ch (A. Testino).

http://dx.doi.org/10.1016/j.apcatb.2015.09.012
0926-3373/

Fouling due to carbon deposition (coking) is considered one of the main reasons for catalyst deactivation during CO methanation and results in decreased catalyst's lifetime. Severe carbon deposition may be induced by a minor fraction of hydrocarbons in the reactive gas mixture like ethylene, acetylene, benzene, etc., as measured in the producer gas of gasification plants [10].

Carbon can be formed by CO disproportionation (also known as Boudouard reaction, Reaction (3)), polymerization and dehydrogenation of hydrocarbons on catalyst's surface (Reaction (4)) or dissociation of hydrocarbons (Reaction (5)). Different types of carbon deposits, with different morphology and reactivity may be formed, namely Cα or carbidic carbon (formation temperature, T_f = 200–400 °C), polymeric or amorphous carbon (T_f = 250–500 °C), C_γ or graphitic carbon (T_f = 150–250 °C), C_v fibers/whiskers (T_f = 300–1000 °C) and C_c graphitic platelets/films (T_f = 500–550 °C) [10,11].

$$2CO \rightarrow C + CO_2 \quad (3)$$

$$C_xH_y + \ldots + C_nH_m \rightarrow \text{high molecular weight hydrocarbons} \rightarrow C_\alpha, C_\beta, C_\gamma + H_2 \quad (4)$$

$$C_xH_y \rightarrow C_\alpha + H_2 + C_nH_m \quad (5)$$

The carbon species can lead to different phenomena on the catalyst surface. Macroscopically, the metallic phase may be encapsulated or detached from the support or the deposited carbon may react forming superficial metal carbides [11,13,14]. Disregarding to its nature, carbon deposition represents a major concern and the preparation of a coking-resistant catalytic materials is a target of paramount importance. In the tentative to mitigate the coking problem, fixed bed reactors were replaced with more expensive fluidized bed reactors [15,16]. Engineered materials have been proposed as well, for example, the introduction of boron in the metallic catalyst and modification of the structural and chemical properties of the support [11,17,18].

To improve the catalyst performance, a second relevant issue has to be addressed: the limited thermal stability *in operando*. The requirement to have catalysts with high active area suggests the use of nanoparticles. It is a matter of fact that nanomaterials have a much lower sintering temperature than analogous bulk materials. Moreover, the exothermic CO methanation reaction, combined with the reducing environment, further promotes nanoparticle sintering. As a result, dispersed Ni nanoparticles sinter together to form larger Ni sponge *in operando*, setting the activity of the catalyst to the level of commercial Ni-Raney, annulling the effort of applying nanoparticles.

The common strategy to mitigate sintering is to disperse Ni particles on a metal oxide support, such as γ-type Al_2O_3 [12,19]. Efforts have been made to enhance the stability of the Ni/Al_2O_3 system, including increasing Ni loadings [20], tuning the reduction temperature [21], adding catalyst promoters [22–25], and developing advanced synthesis methods [26–28]. Moreover, calculations showed that *in operando* also Al_2O_3 undergoes modification of its physico-chemical properties, such as reduction of the acidic sites and specific surface area [19]. Today, Ni-based catalysts with anti-coking and anti-sintering properties are rarely available [29–31] and an *ad-hoc* catalyst for CO methanation is still not existing.

Recently, we developed the continuous synthesis for Ni nanoparticles (NPs) using the Segmented Flow Tubular Reactor (SFTR) [32]. We demonstrated that the method allows the continuous production of nanoparticles with tailored properties and in quantity of about 300 g day^{-1}, with constant quality. The produced powders were tested as catalyst for the methanation of CO and interesting activities were demonstrated. We also addressed the sintering behavior of the material as one of the major drawback.

In this paper we report on our strategy in order to produce an advanced catalyst with anti-coking and anti-sintering properties. The nanoparticles surface is protected with a second material, which (i) is able to prevent sintering, (ii) is gas permeable, and (iii) protects the particle surface from coking.

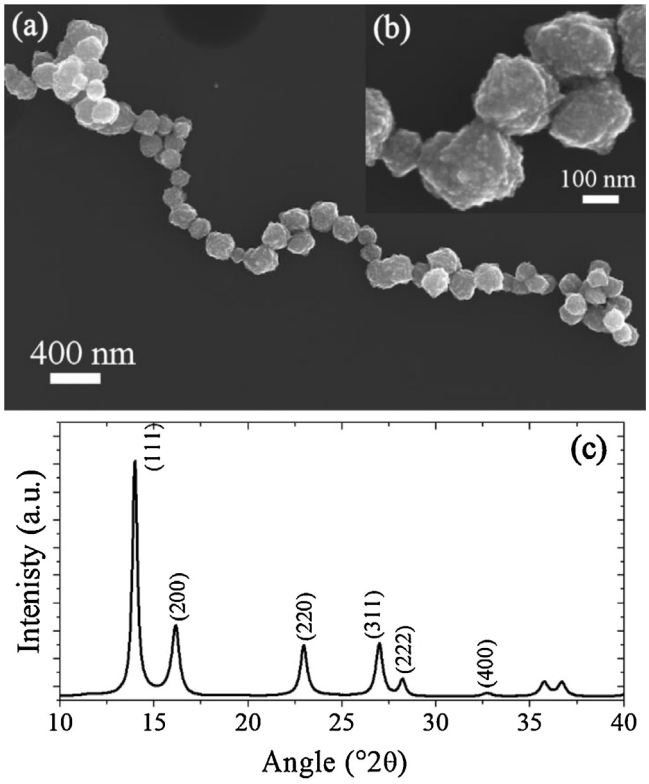

Fig. 1. (a) FE-SEM micrograph as prepared Ni NPs. At higher magnification (b) the particle substructure is highlighted. Synchrotron XRD pattern (25 keV) of the pure Ni *fcc* crystalline structure.

The possibility to avoid sintering by coating has been recently reported for some materials [33–36] and applications [37–40]. However, this strategy was never reported in literature for Ni nanoparticles used as CO methanation catalyst. Here, we present the synthesis, characterization, and catalytic performance of Ni nanoparticles (core) coated with microporous SiO_2 (shell). The obtained core–shell catalyst (*Ni@m-SiO$_2$*) provides a strategic guideline towards the production of advanced catalysts with improved activity and stability.

2. Experimental

2.1. Materials

Nickel chloride hexahydrate ($NiCl_2{\cdot}6H_2O$, >98%), hydrazine monohydrate ($N_2H_4{\cdot}H_2O$, 65%, reagent grade 98%), sodium hydroxide (NaOH, >98%), ethylene glycol (EG, puriss. p.a. ≥99.5%), n-dodecane (*n*-C_{12}, reagent grade, ≥99%), ammonia (NH_3, 29%), cetyl trimethylammonium bromide (CTAB, ≥99%), ammonium nitrate (NH_4NO_3, ≥99%) and tetraethyl orthosilicate (TEOS, 98%) were obtained from Sigma–Aldrich and used as received without further purification. Ethanol and acetone used for powder washing purpose were reagent grade and obtained from VWR. γ-Al_2O_3 (Sasol Puralox) was used to dilute the material for the catalytic tests.

2.2. Ni nanoparticles (core) synthesis

The synthesis of the Ni NPs was performed in the SFTR as described in our previous work [32]. Briefly, the reaction was performed at 60 °C using 0.4 M $NiCl_2{\cdot}6H_2O$ and molar N_2H_4/Ni ratio of 3. The reaction time was 12 min. At the end of the synthesis,

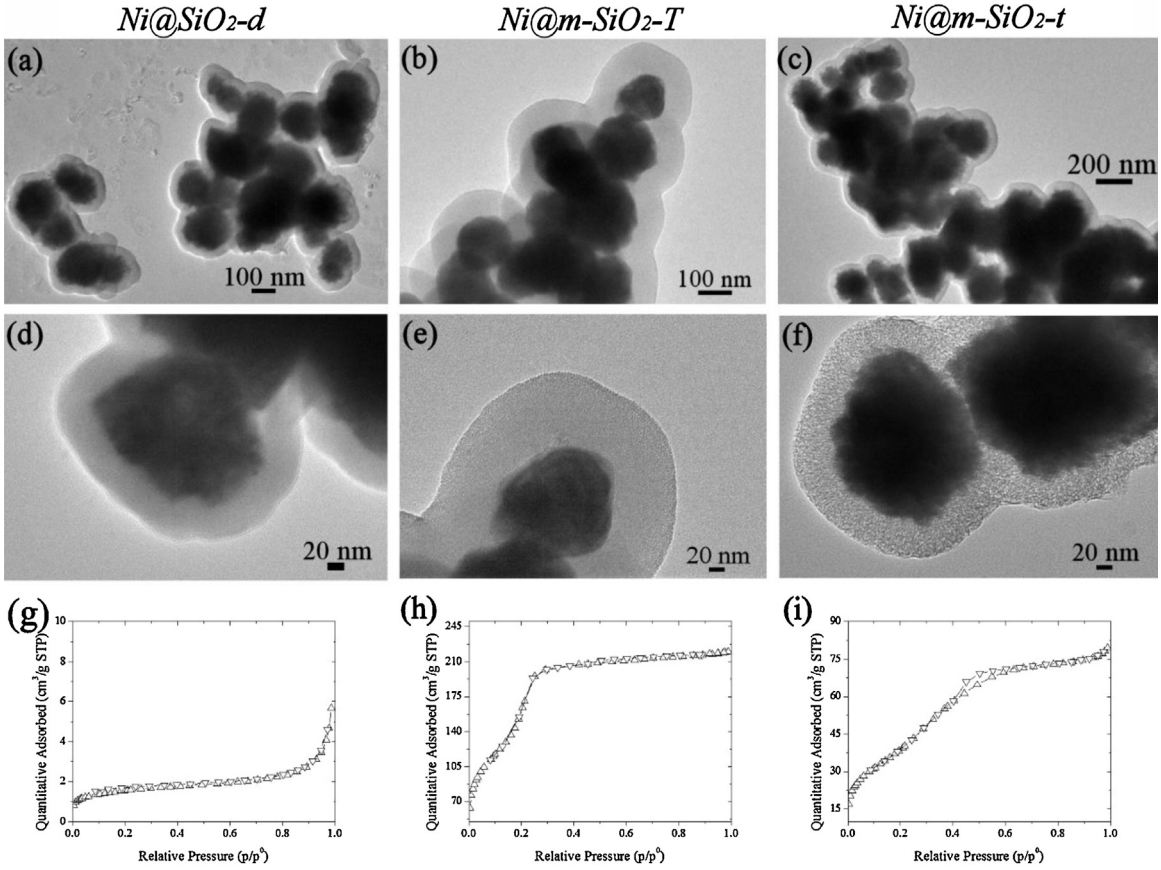

Fig. 2. (a)–(c) and (d)–(f) low and high magnification TEM micrographs, respectively, and (g–i) N_2 physisorption isotherms for the samples *Ni@SiO$_2$-d*, *Ni@m-SiO$_2$-T* and *Ni@m-SiO$_2$-t*.

the particles were washed three times with ethanol and once with acetone.

2.3. Silica layer (shell) synthesis

Three series of samples were prepared: dense silica coated Ni NPs (*Ni@SiO$_2$-d*), thin microporous silica coated NPs (*Ni@m-SiO$_2$-t*), and thick microporous silica coated Ni NPs (*Ni@m-SiO$_2$-T*).

Ni@SiO$_2$-d: 150 mg of Ni NPs were placed in a solution of ethanol (400 mL), water (8 mL) and ammonia solution (29%, 18 mL) and finally sonicated for 5 min (Sonics—VIBRA CELL, VCX130, 130 W 20 kHz, 100% power). Then TEOS was added to the mixture (1.6 mL) and the reaction was maintained at room temperature (RT) for 19 h under vigorous mechanical stirring. After the reaction, the particles were washed three times with ethanol and once with acetone, retrieving the product by a permanent magnet and sonicating between each washing step. The magnetic retrieval allows the separation between the magnetic core–shell particles from the pure silica particles. Finally, the powders were dried in air at RT and stored in closed vials.

Ni@m-SiO$_2$-t and *Ni@m-SiO$_2$-T*: 200 mg of Ni NPs were dispersed in a solution of ethanol (150 mL), water (100 mL) and ammonia solution (29%, 2 mL). Finally, 450 mg of CTAB were added to the mixture. The suspension was sonicated for 5 min and then was placed in a three neck flask under vigorous mechanical stirring at RT for 30 min. Then TEOS (1.5 mL or 0.15 mL for samples *Ni@m-SiO$_2$-T* or *Ni@m-SiO$_2$-t*, respectively) was added. The reaction was carried out for 6 h at 60 °C. The product was magnetically retrieved and washed twice with ethanol. The templating agent, was removed by washing twice with a NH_4NO_3/ethanol solution (6 g L^{-1}) at RT [40]. Finally the powders were dried in air and stored in closed vials.

2.4. Catalyst preparation

The silica coated NPs were diluted with γ-Al_2O_3 in order to keep the amount of Ni and the gas hourly space velocity (GHSP) constant. The powders were placed in a glass vial with 15 mL of isopropanol and sonicated (Sonics—VIBRA CELL, VCX130, 130 W 20 kHz, 100% power, 5 min). After sedimentation, the solvent was removed and the powder dried at RT. For comparative reasons, a catalyst based on uncoated Ni NPs diluted with γ-Al_2O_3 was prepared as well.

2.5. Material characterization

X-ray powder diffraction (XRD) patterns were collected at the MS-X04SA beamline (SLS-PSI) using a 0.3 mm capillary at the energy of 25 keV [41].

Transmission electron microscopy (TEM) studies were performed on a JEOL 2010 with an acceleration voltage of 200 keV, equipped with a LaB_6 filament, an Oxford Instrument energy dispersive X-ray spectrometer (EDS), using INCA software and a CCD camera (Orius from GATAN). A single tilt holder was used. The powders were suspended in isopropanol, and a 5 μL drop of this suspension was deposited on a holey carbon film supported on 3 mm copper grid for TEM investigation.

Field Emission Scanning Electron Microscopy (FE-SEM) investigations were performed using a Zeiss SUPRA 40 VP instrument working at 20 keV, equipped with an energy dispersive X-ray spectrometer (EDX-OXFORD "INCA Energy 450 × 3") for microanalysis.

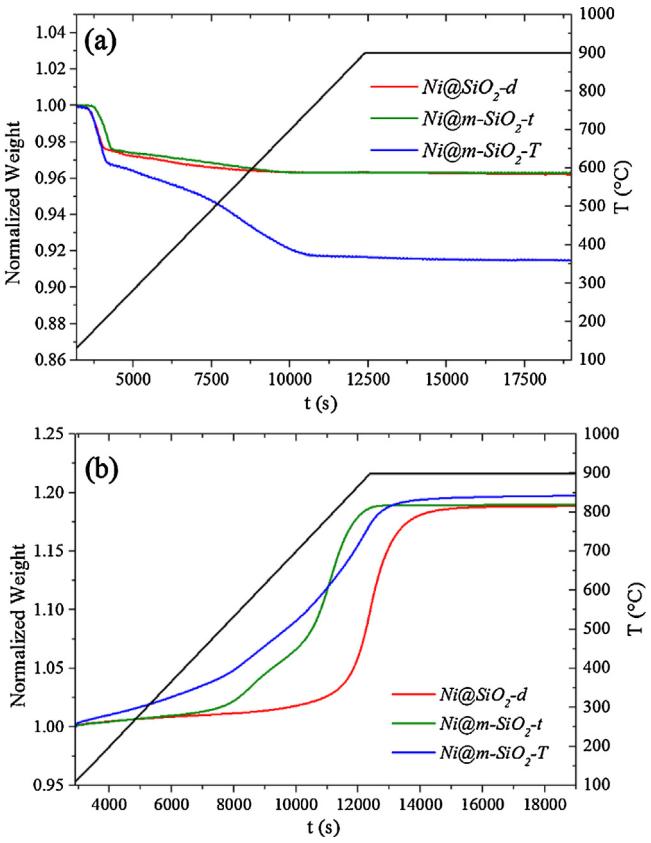

Fig. 3. Thermogravimetric analyses done under (a) reducing and (b) oxidizing atmosphere. The treatments in (b) were done after the treatment (a). The weights are normalized to the mass of dried samples at 110 °C for 30 min.

The *Specific Surface Area* (SSA, BET method [41]) and the pore size distribution (BJH method, desorption branch [42]) were determined by nitrogen physisorption using a Micromeritics Tristar II 3020 working at 77 K, after evacuation of the sample at 110 °C overnight.

Thermogravimetric analyses (TGA) were carried out with a Mettler Toledo SDTA/TGA 1 system using air or 4 vol% H_2 (balance Ar) as reactive gas at the flow rate of 20 mL min^{-1}. For all the experiments, the weight of the sample was recorded between RT and 900 °C.

The catalytic performance of the prepared materials for CO methanation was evaluated in a fixed bed reactor operating at atmospheric pressure according to the procedure described in reference [32]. The stability tests were conducted in the presence of 25 vol.% H_2/5 vol.% CO/2000 ppm C_2H_4, (bal. N_2) with a GHSV = 60000 mL g^{-1} s^{-1} to eventually promote coking, maintaining constant both the gas flow conditions and the catalyst bed volume in all the experiments. Before each stability test the catalyst was pretreated at 250 °C (heating rate 20 °C min^{-1}) in 5 vol% H_2 (bal. N_2) and then at 500 °C (heating rate 5 °C min^{-1}) in 25 vol% H_2 and 5 vol% CO (balance N_2).

For the stability test, the temperature was lowered in order to achieve ~55% of CO conversion and the gas mixture was introduced in the reactor. The oven set temperatures for the stability tests were 375 °C and 340 °C for uncoated Ni NPs and sample *Ni@m-SiO$_2$-t*, respectively. The CO conversion (x_{co}) data are reported as

$$x_{co} = 100\frac{(C_{co}^{in} - C_{co}^{out})}{C_{co}^{in}}$$

where C_{co}^{in} and C_{co}^{out} are the concentration of CO in the inflow and outflow, respectively. Carbon deposits were estimated from CO_2 evolution during temperature programmed oxidation (TPO) with 10 vol% O_2 (balance N_2) in the temperature range 40–800 °C (5 °C min^{-1}).

3. Results and discussion

3.1. Characterization of the as-prepared catalyst

Ni NPs were obtained from a single run experiment in the SFTR from which 10 g of product were obtained. Ni NPs are uniformly spherical with an average diameter of 169 ± 20 nm (Fig. 1a). Higher magnification micrographs disclose the particles substructure, which are aggregates of smaller crystals (Fig. 1b) [32]. The metallic *fcc* structure (JCPDS No. 04-0485) of the particles was confirmed by X-ray diffraction, (Fig. 1c); no secondary phases were detected. All the coated samples were prepared using this starting material.

Tuning the coating protocol is possible to tailor the thickness of the layer. Fig. 2(a–c) shows the TEM micrographs for samples *Ni@SiO$_2$-d*, *Ni@m-SiO$_2$-T*, and *Ni@m-SiO$_2$-t*, respectively. The core–shell structure is evinced by the difference in contrast between the outer silica layer (lighter) and the inner Ni core (darker). Fig. S1 (Supporting information) show the EDX spectra of the coated particles. The shell is of about 30–40 nm for samples *Ni@SiO$_2$-d* and *Ni@m-SiO$_2$-t* and of about 80 nm for sample *Ni@m-SiO$_2$-T*. Uncoated Ni NPs were not detected for the thin layer samples, confirming the reliability of the coating procedure. Nevertheless, for the sample *Ni@m-SiO$_2$-T*, due to the large amount of TEOS, pure silica particles have been found attached to coated core–shell particles and some Ni NPs particles were not completely coated. (Fig. S2, Supporting information)

By TEM it is not trivial to identify the porous structure of the silica shell. Nevertheless, a denser silica layer is found for sample *Ni@SiO$_2$-d* (Fig. 2d) in comparison to sample *Ni@m-SiO$_2$-t* where the presence of a randomly organized porous structure might be speculated (Fig. 2f). The porosity of the silica layer was investigated by N_2 physisorption at 77 K. Fig. 2(g–i) shows the isotherms for samples *Ni@SiO$_2$-d*, *Ni@m-SiO$_2$-T* and *Ni@m-SiO$_2$-t*.

Sample *Ni@SiO$_2$-d*, Fig. 2g, presents a type II isotherm [43,44] typical for non-porous materials. The SSA was 5.5 m^2/g in agreement with the value reported for bare Ni NPs (5.7 m^2/g) [32], confirming the presence of a dense non-porous SiO_2 layer. Samples *Ni@m-SiO$_2$-T* and *Ni@m-SiO$_2$-t* (Fig. 2h–i) show type IV isotherm with relevant microporous contribution, a SSA of 529 and 136 m^2/g and an average pore size of 2.1 and 3.0 nm, respectively. These results are in agreement with the literature for cylindrical pores [45,46]. The different average pore size and their organization were tuned by the CTAB/TEOS ratio applied in the synthesis protocol [47].

In order to evaluate the permeability of the SiO_2 layers to reactive gases, the samples weight was measured against temperature by TGA, under reducing and oxidizing atmosphere (Fig. 3). Under reducing atmosphere (Fig. 3a), a stable sample weight is obtained at about 750 °C for all samples. The first weight loss (25–230 °C) is attributed to humidity [48] whereas the second contribution at T > 220 °C can be assigned to the transformation of small amount of NiO and/or $Ni(OH)_2$ to Ni, as previously reported [32]. The two samples coated with the thin layer show similar weight loss, confirming that the templating agent used in the sample *Ni@m-SiO$_2$-t* was properly removed by washing. Sample *Ni@m-SiO$_2$-T* shows a bigger weight loss due to a higher content of NiO, in agreement with the non-optimal SiO_2 coating (Fig. S2, Supporting information) which is not able to protect the product from oxidation.

Fig. 3b reports on the weight variation of the samples treated under oxidizing atmosphere after the treatment under reducing atmosphere: the weight increases with temperature for all samples is in excellent agreement with the oxidation from Ni to NiO. Nevertheless, the different nature of the coating induces differences in the oxidation kinetic. The signal for the *Ni@m-SiO$_2$-T* is rather diffuse and starts at low temperature, as a consequence of the poor quality of the coating: the fraction of uncoated Ni particles start to be oxidized at T < 200 °C. Sample *Ni@m-SiO$_2$-t* shows limited oxidation at room temperature and a rather fast reaction at higher temperatures (>300 °C); two oxidation processes might be speculated at 330 and 630 °C that might be attributed to Ni surface and Ni bulk oxidation, respectively. Sample *Ni@SiO$_2$-d* shows a single oxidation which is completed at 900 °C.

These results are in agreement with the N_2 physisorption measurements considering that N_2 and O_2 have a similar size (3.8 and 3.5 Å, respectively). In the sample *Ni@m-SiO$_2$-t* these gases can diffuse in the porous structure at relatively low temperature and reach the Ni core. Sample *Ni@SiO$_2$-d* has no available pores for gas diffusion and hence oxidation can occur only at high temperature when oxygen can diffuse through the solid SiO_2 layers (solid state diffusion). It is worth noting that CO, CO_2, and CH_4, which are the gases involved in the reaction of interest (Reactions (1) and (2)), have a size similar to N_2 (3.76, 3.94, and 3.80 Å, respectively) [49,50] and therefore similar diffusion on the porous structure is expected. H_2O has a smaller size (2.75 Å).

Dense and porous layers are H_2-permeable because of the smaller size of H_2 (2.8 Å) with respect to O_2 and N_2. H_2 permeability is a relevant property because the catalyst might be regenerated or activated by a treatment under reducing atmosphere. Similar diffusion selectivity (H_2 vs. CO) was reported for thin dense SiO_2 layers [51].

It can be concluded that the combination of TEM, N_2-physisorption and TGA experiments under controlled atmosphere allowed the characterization of the physico-chemical properties of the coating. The porous structure of the sample *Ni@m-SiO$_2$-t* offers channels which are one order of magnitude larger than the size of the gaseous species considered in the reaction of interest; at the same time coating is able to prevent surface oxidation at RT. The sample *Ni@m-SiO$_2$-t* shows the best properties since (i) no signal related to uncoated particle is detected and the porous layer is (ii) H_2- and (iii) CO-, CO_2- and CH_4-permeable.

Table 1
Sample composition calculated from the TGA measurement of Fig. 3.

	Ni@SiO$_2$-d	*Ni@m-SiO$_2$-t*	*Ni@m-SiO$_2$-T*
Ni	84.9%	85.6%	84.8%
NiO	1.4%	1.2%	5.1%
SiO_2	11.4%	10.9%	7.0%
Water	2.2%	2.3%	3.1%

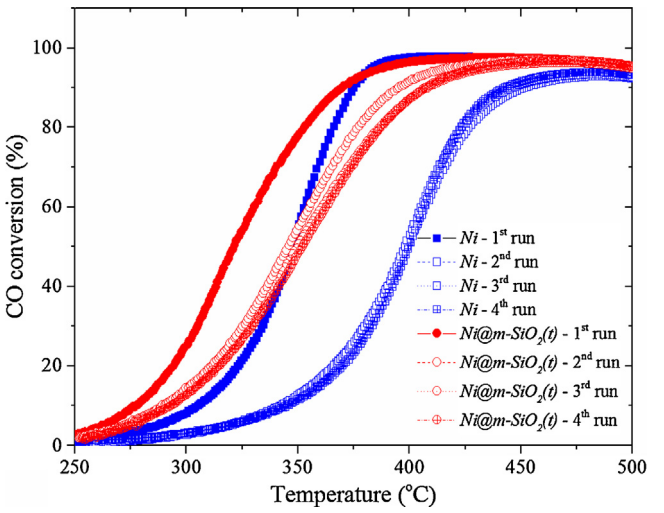

Fig. 4. CO conversion against temperature for the bare Ni NPs (blue) and the sample *Ni@m-SiO$_2$-t* (red). Four runs are reported in the figure as described in the label. Runs 1 and 3 refer to heating up whereas runs 2 and 4 refer to cooling down. (For interpretation of the references to colour in this figure legend, the reader is referred to the web version of this article.)

From the TGA curve (Fig. 3) it is possible to estimate the sample composition [32], as summarized in Table 1. For the thin layer samples, the amount of SiO_2 calculated is in excellent agreement with the particles geometry reported in Fig. 2. The low amount of SiO_2 in the sample *Ni@m-SiO$_2$-T*, despite the amount of TEOS used in the synthesis protocol, can be again attributed to the non-optimal coating: the product is magnetically retrieved after the washing treatments and most of the SiO_2 in form of particles without a magnetic core were washed away. The difference among the two thin coated samples is due to the porous structure of the shell only. The comparative study between the *Ni@m-SiO$_2$-t* and the uncoated Ni NPs offers an ideal case to assess the effectiveness of the coating as anti-sintering, anti-coking, and the catalytic activity performance.

3.2. CO methanation: catalytic behavior of the materials

The catalytic performance of the bare Ni NPs and *Ni@m-SiO$_2$-t* core–shell particles, diluted with γ-Al_2O_3, were evaluated for CO methanation. Fig. 4 shows the temperature programmed methanation runs, following two catalytic cycles (heating-up and cooling-down). Fig. S3 (Supporting information) reports the CO conversion and CH_4 yield for the three coated samples. The catalytic performance of the bare Ni NPs were previously reported [32]. Briefly, the material is very active during the first run but, because of sintering, the activity strongly decreases already during the first cooling-down. The following cycle (runs 3 and 4) overlaps

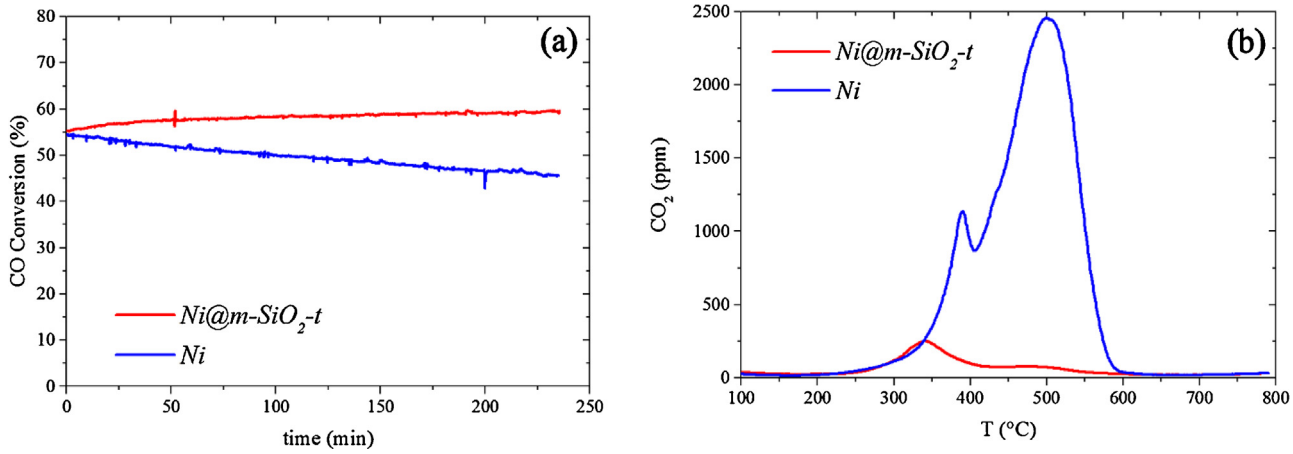

Fig. 5. (a) CO conversion against time for the bare Ni NPs and the sample *Ni@m-SiO$_2$-t* in the presence of C_2H_4 The catalyst temperatures were tuned to attain the same initial conversion and then kept constant over time. (b) TPO of the Ni NPs and the sample *Ni@m-SiO$_2$-t*.

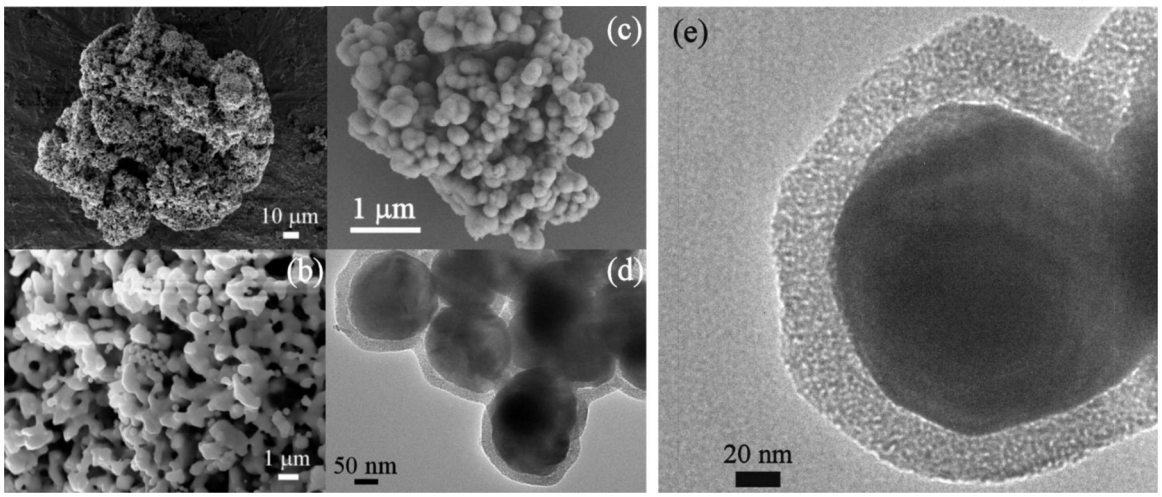

Fig. 6. SEM (a-c) and TEM (d) micrographs of the catalyst after the catalytic tests of Fig. 4. (a) and (b) bare Ni particles and low and high magnification. (c) and (d) the *Ni@m-SiO$_2$-t* sample. In (e) the higher magnification of (d) is shown.

the first cooling down curve (run 2). The 50% CO conversion in the first run is obtained at 346 °C, whereas it corresponds to 400 °C in the following runs. The lost in material activity can be estimated considering the amplitude of the hysteresis in the first catalytic cycle, which corresponds to 60 °C at 80% CO conversion.

To some extent the behavior of the *Ni@m-SiO$_2$-t* sample is similar. During the first run the material is very active, attaining the 50% CO conversion at 321 °C, thus more active than the bare particles. It can be argued that also during the first run, when the temperature is higher than 250 °C, the bare particles are already loosing activity because of poisoning or surface area decrease. In the second run the material is less active but the 50% CO conversion is attained almost at the same temperature of the first run of the bare particles. The following cycle shows a stable behavior. For this material the amplitude of the first cycle hysteresis at 80% CO conversion is of about 20 °C, thus 1/3 of the value obtained for the bare Ni NPs.

Fig. 5a shows the evolution of CO conversion over time for the Ni NPs and *Ni@m-SiO$_2$-t* core–shell particles when 2000 ppm C_2H_4 was present in the feed gas. The temperature of the catalyst was tuned to attain the same initial conversion, namely 375 °C and 340 °C for the Ni NPs and *Ni@m-SiO$_2$-t* core–shell particles, respectively, and then kept constant over time.

Ni NPs lost approximately 18% of its initial activity within 4 h. In contrast, a significant improvement in the stability was observed on the sample *Ni@m-SiO$_2$-t* with a constant conversion over the 4 h test.

After the long term catalytic test, the temperature programmed oxidation (TPO) profiles of the samples were recorded. Fig. 5b shows notably different CO_2 desorption peaks, corresponding to different C deposition contributions. No graphitic or filamentous carbon was detected since no peaks in the temperature region above 600 °C were revealed. These types of carbon depositions are common during CO methanation for conventional catalysts at fixed-bed conditions.

In the case of Ni NPs, at least two peaks dominate the lower temperature range. The peak at low temperature (250–450 °C) [52] is attributed to nickel carbide whereas the prominent peak in the temperature range of 400–600 °C can be assigned to amorphous carbon species of C [53]. This second peak practically vanishes in the sample *Ni@m-SiO$_2$(t)*. Amorphous carbon deposition is considered the main factor for catalyst deactivation during the methanation process of CO.

After the catalytic test, the samples have been characterized by means of electron microscopy in order to check the sintering behavior and the carbon deposition. In Fig. 6 the results for bare Ni (Fig. 6a and b) and *Ni@m-SiO2-t* (Fig. 6c and d) are shown.

As previously reported, uncoated particles underwent massive sintering, invalidating the effort of using nanoparticles [32]. Fig. 6(a

and b) shows the sponge-like structure obtained *in operando* for the bare Ni NPs. On the contrary the long term catalytic tests have almost no effect on the macroscopic structure of the sample *Ni@m-SiO_2-t*. Comparing Fig. 2f and Fig. 6d, it can be observed that the rough surface of the pristine particles (Fig. 2f) becomes smooth after the catalytic test. This modification is due to the local crystallization of the particles which have a substructure before the thermal treatment and become a single crystal upon treatment. The limited loss in activity, highlighted in Fig. 4, might be associated to this restructuring and the associated limited shrinkage left a thin empty space of about 2–3 nm (*hollow corona*) between the core and the shell (Fig. 6e).

Nevertheless, the SiO_2 layer prevents the massive sintering (Fig. 6d) and surface area of the catalyst did not collapse as found for the bare Ni particles (Fig. 6b).

The reason why the sample *Ni@m-SiO_2-t* does not show amorphous carbon deposition might be attributed to the space between the Ni core and the SiO_2 shell which is limited to the *hollow corona* (Fig. 6e): if carbon deposition occurs, it has to be close to the reactive Ni surface within the *hollow corona*, where it could be transformed back into gaseous species. Anyway, no space is available for substantial carbon accumulation on the Ni core surface.

4. Conclusions

The rapid sintering of Ni NPs combined with the poisoning effect of carbon species deposition on the catalyst surface, from one hand hinder the applicability of nanomaterials in fixed bed reactors and on the other hand promote the development of expensive strategies to remove the deposited carbon layers, such as the application of fluidized bed reactors.

The synthesis of engineered materials for catalytic applications addressing these two specific problems, have been achieved. The obtained core–shell particles, composed by a nanometric catalytically active Ni core protected by a microporous SiO_2 shell which confers anti-sintering and anti-coking properties, were fully characterized. The results demonstrated that the material is stable against time and temperature. Carbon deposition is almost absent even in the presence of 2000 ppm of C_2H_4 and the material does no sinter *in operando*. The synthesis pathway and method chosen for the material preparation allow the production of relevant quantities for testing in pilot plant or larger test facilities with fixed-bed reactors and it could be market competitive.

The maximum CO conversion of 96% was obtained at 440 °C and the material does not sinter at 500 °C. The microporous 30–40 nm microporous SiO_2 layer does not hinder the gas permeation. From the scientific point of view, the outstanding performance of the produced core–shell catalyst (*Ni@m-SiO_2*) provides a strategic guideline towards the production of advanced catalysts with improved activity and stability.

Author contribution

MAL carry out the synthesis of the material and substantially contributed to the manuscript preparation. AT wrote the paper and coordinates the scientific activity. AK and CP did the catalytic and microscopic characterization of the samples, respectively, and contributed to the manuscript preparation. CL provided the financial support and substantially contributed to the paper reviewing.

Conflicts of interest

The authors declare no conflict of interest.

Acknowledgements

We thank Antonio Cervellino and the Materials Science MS-X04SA beamline SLS-PSI for the high resolution XRD analysis. MAL thank Paola Riani and Fabio Canepa for the useful discussions. AT thank Paul Bowen for the SFTR technology.

Appendix A. Supplementary data

Supplementary data associated with this article can be found, in the online version, at http://dx.doi.org/10.1016/j.apcatb.2015.09.012.

References

[1] T.J. Schildhauer, Synth. Nat. Gas from Coal, Dry biomass Power-to-Gas Applications, Wiley & Sons, New York, 2015.
[2] J. Kopyscinski, T.J. Schildhauer, S.M.A. Biollaz, Fuel 2010 (1763) 89.
[3] J. Gao, C. Jia, J. Li, F. Gu, G. Xu, Z. Zhong, F. Su, Ind. Eng. Chem. Res. 51 (2012) 10345.
[4] A. Zhao, W. Ying, H. Zhang, M. Hongfang, D. Fang, J. Nat. Gas. Chem. 21 (2012) 170.
[5] J. Gao, C. Jia, M. Zhang, F. Gu, G. Xu, F. Su, Catal. Sci. Technol. 3 (2013) 2009.
[6] S. Tada, R. Kikuchi, A. Takagaki, T. Sugawara, S.T. Oyama, K. Urasaki, S. Satokawa, Appl. Catal. B Environ. 140 (2013) 258.
[7] J. Zarfl, D. Ferri, T.J. Schildhauer, J. Wambach, A. Wokaun, Appl. Catal. A: Gen. 495 (2015) 104.
[8] S. Eckle, Y. Denkwitz, R.J. Behm, J. Catal. 269 (2010) 255.
[9] C.S. Chen, J.H. Lin, J.H. You, K.H. Yang, J. Phys. Chem. A 114 (2010) 3773, http://dx.doi.org/10.1021/jp904434e.
[10] M.C. Seeman, T.J. Schildhauer, S.M.A. Biollaz, Ind. Eng. Chem. Res. 49 (2010) 7034.
[11] L. Guczi, A. Erdohelyi, Catalysis for Alternative Energy Generation, Springer, New York, USA, 2012.
[12] C.H. Bartholomew, Catal. Rev. 24 (1982) 67.
[13] Czekaj, F. Loviat, F. Raimondi, S.M.A. Biollaz, A. Wokaun, Appl. Catal. A Gen. 329 (2007) 68.
[14] J. Kopyscinski, T.J. Schildhauer, S.M.A. Biollaz, Chem. Eng. Sci. 66 (2011) 1612.
[15] J. Kopyscinski, T.J. Schildhauer, S.M.A. Biollaz, Ind. Eng. Chem. Res. 50 (2011) 2781–2790.
[16] M.C. Seemann, T.J. Schildhauer, S.M.A. Biollaz, Ind. Eng. Chem. Res. 49 (2010) 7034.
[17] A. Kambolis, H. Matralis, A. Trovarelli, C. Papadopoulou, Appl. Catal. A Gen. 377 (2010) 16.
[18] A. Fouskas, M. Kollia, A. Kambolis, C. Papadopoulou, H. Matralis, Appl. Catal. A Gen. 474 (2014) 125.
[19] J. Gao, C. Jia, J. Li, M. Zhang, F. Gu, G. Xu, Z. Zhong, F. Su, J. Eng. Chem. 22 (2013) 919.
[20] S. Hwang, J. Lee, U.G. Hong, J.G. Seo, J.C. Jung, D.J. Koh, H. Lim, C. Byun, I.K. Song, J. Ind. Eng. Chem. 17 (2011) 154.
[21] C.W. Hu, J. Yao, H.Q. Yang, Y. Chen, A.M. Tian, J. Catal. 166 (1997) 1.
[22] D.C. Hu, J.J. Gao, Y. Ping, L.H. Jia, P. Gunawan, Z.Y. Zhong, G.W. Xu, F.N. Gu, F.B. Su, Ind. Eng. Chem. Res. 51 (2012) 4875.
[23] A.M. Zhao, W.Y. Ying, H.T. Zhang, H.F. Ma, D.Y. Fang, J. Nat. Gas. Chem. 21 (2012) 170.
[24] S. Hwang, J. Lee, U.G. Hong, J.C. Jung, D.J. Koh, H. Lim, C. Byun, I.K. Song, J. Ind. Eng. Chem. 18 (2012) 243.
[25] A. Kambolis, D. Ferri, Y. Lu, S.N. Yannopoulos, S. Pokrant, D. Rentsch, O. Kröcher, ChemCatChem (2015), http://dx.doi.org/10.1002/cctc.201500567.
[26] S. Hwang, J. Lee, U.G. Hong, J.G. Seo, J.C. Jung, D.J. Koh, H. Lim, C. Byun, I.K. Song, J. Ind. Eng. Chem. 17 (2011) 154.
[27] A.M. Zhao, W.Y. Ying, H.T. Zhang, H.F. Ma, D.Y. Fang, Catal. Commun. 17 (2012) 34.
[28] S.L. Ma, Y.S. Tan, Y.Z. Han, J. Nat. Gas. Chem. 20 (2011) 435.
[29] J. Newnham, K. Mantri, M.H. Amin, J. Tardio, S.K. Bhargava, Int. J. Hydrogen Energy 37 (2012) 1454.
[30] Z. Li, L. Mo, Y. Kathiraser, S. Kawi, ACS Catal. 4 (2014) 1526.
[31] J.C. Park, J.U. Bang, J. Lee, C.H. Ko, H. Song, J. Mater. Chem. 20 (2010) 1239, http://dx.doi.org/10.1039/B918446E.
[32] M.A. Lucchini, A. Testino, C. Ludwig, A. Kambolis, M. El-Kazzi, A. Cervellino, P. Riani, F. Canepa, Appl. Catal. B Environ. 156–157 (2014) 404.
[33] M. Cargnello, J.J. Delgado Jaén, J.C. Hernández Garrido, K. Bakhmutsky, T. Montini, J.J. Calvino Gámez, R.J. Gorte, P. Fornasiero, Science 337 (2012) 713.
[34] Y. Deng, Y. Cai, Z. Sun, J. Liu, C. Liu, J. Wei, W. Li, C. Liu, Y. Wang, D. Zhao, JACS 132 (2010) 8466.
[35] T. Zhang, H. Zhao, S. He, K. Liu, H. Liu, Y. Yin, C. Gao, ACS Nano 8 (2014) 7297.
[36] W. Li, D. Zhao, Adv. Mater. 25 (2013) 142.
[37] Y. Deng, D. Qi, C. Deng, X. Zhang, D. Zhao, JACS 130 (2008) 28.
[38] X. Guo, Y. Deng, D. Gu, R. Che, D. Zhao, J. Mater. Chem. 19 (2009) 6706.
[39] R. Xie, C. Wang, L. Xia, H. Wang, T. Zhao, Y. Sun, Catal. Lett. 144 (2014) 516, http://dx.doi.org/10.1007/s10562-013-1187-z.

[40] J. Yang, F. Zhang, Y. Chen, S. Qian, P. Hu, W. Li, Y. Deng, Y. Fang, L. Han, M. Luqman, D. Zhao, Chem. Commun. 47 (2011) 11618.
[41] P.R. Willmott, D. Meister, S.J. Leake, M. Lange, A. Bergamaschi, M. Böge, M. Calvi, C. Cancellieri, N. Casati, A. Cervellino, Q. Chen, C. David, U. Flechsig, F. Gozzo, B. Henrich, S. Jäggi-Spielmann, B. Jakob, I. Kalichava, P. Karvinen, J. Krempasky, A. Lüdeke, R. Lüscher, S. Maag, C. Quitmann, M.L. Reinle-Schmitt, T. Schmidt, B. Schmitt, A. Streun, I. Vartiainen, M. Vitins, X. Wang, R. Wullschleger, J. Synchrotron Radiat. 20 (2013) 667.
[42] S. Brunauer, P. Emmett, E. Teller, J. Am. Chem. Soc. 60 (1938) 309.
[43] E. Barrett, L. Joyner, P. Halenda, J. Am. Chem. Soc. 73 (1951) 373.
[44] S.J. Gregg, K.S.W. Sing, Adsorption, Surface Area and Porosity, Academic Press, London–New York, 1982.
[45] Y. Deng, Y. Cai, Z. Sun, J. Liu, C. Liu, J. Wei, W. Li, C. Liu, Y. Wang, D. Zhao, J. Am. Chem. Soc. 132 (2010) 8466.
[46] W. Li, D. Zhao, Adv. Mater. 25 (2013) 142.
[47] Z. Teng, G. Zheng, Y. Dou, W. Li, C.Y. Mou, X. Zhang, A.M. Asiri, D. Zhao, Angew. Chem. Int. Ed. 51 (2012) 2173.
[48] L.L. Hench, J.K. West, Chem. Rev. 90 (2000) 33.
[49] C. Huber, U. Beyerle, M. Leuenberger, J. Schwander, R. Kipfer, R. Spahni, J.P. Severinghaus, K. Weiler, Earth Planet Sci. Lett. 243 (2006) 61.
[50] A.K. Pabby, S.S.H. Rizvi, A.M. Sastre Requenza, Handbook of Membrane Separation: Chemical, Pharmaceutical, Food and Biotechnological Applications, CRC Press, 2009.
[51] D. Lee, Ph.D Thesis, Virginia Tech, 2009, 2015.
[52] R.P.W.J. Struis, D. Bachelin, C. Ludwig, A. Wokaun, J. Phys. Chem. 113 (2009) 2443.
[53] I. Czekaj, F. Loviat, F. Raimondi, J. Wambach, S. Biollaz, A. Wokaun, Appl. Catal. A: Gen. 329 (2007) 68.